# SRN: Side-output Residual Network for Object Reflection Symmetry Detection and Beyond

Wei Ke, Student Member, IEEE, Jie Chen, Member, IEEE, Jianbin Jiao, Member, IEEE, Guoying Zhao, Senior Member, IEEE, and Qixiang Ye, Senior Member, IEEE

Abstract—In this paper, we establish a baseline for object reflection symmetry detection in complex backgrounds by presenting a new benchmark and an end-to-end deep learning approach, opening up a promising direction for symmetry detection in the wild. The new benchmark, Sym-PASCAL, spans challenges including object diversity, multi-objects, part-invisibility, and various complex backgrounds that are far beyond those in existing datasets. The end-to-end deep learning approach, referred to as a side-output residual network (SRN), leverages the output residual units (RUs) to fit the errors between the object ground-truth symmetry and the side-outputs of multiple stages. By cascading RUs in a deep-to-shallow manner, SRN exploits the 'flow' of errors among multiple stages to address the challenges of fitting complex output with limited convolutional layers, suppressing the complex backgrounds, and effectively matching object symmetry at different scales. SRN is further upgraded to a multi-task side-output residual network (MT-SRN) for joint symmetry and edge detection, demonstrating its generality to image-to-mask learning tasks. Experimental results validate both the challenging aspects of Sym-PASCAL benchmark related to real-world images and the state-of-the-art performance of the proposed SRN approach.

Index Terms—Side-output residual network, object reflection symmetry detection, edge detection, multi-task deep learning.

### 1 Introduction

RECTION symmetry is an inherent visual property of natural objects. Object can be abstracted into descriptive and interpretable curves. Such curves constitute a continuous decomposition of object shapes [1], [2], providing discriminative cues for object representation and recognition. Reflection symmetry has been used to produce features and/or spatial constraints and applied to image segmentation [3], foreground extraction [4], object proposal [5], object detection [6], and text-line detection [7].

Early symmetry detection, often referred to as skeleton extraction, usually involves binary images [8], [9]. In recent years, symmetry detection has addressed processing color images [10], [11], [12], but remains limited to cropped image patches with little background. This limitation is partially due to the lack of fundamental benchmarks, considering that most existing symmetry detection datasets, *e.g.*, SYMMAX [13], WH-SYMMAX [14], SK506 [15], and SK-LARGE [16], lack either object-level annotation or the in-the-wild settings, *i.e.*, multi-objects, part-invisibility, and various complex backgrounds.

In this paper, we present a new challenging benchmark with complex backgrounds, and an end-to-end deep symmetry detection approach that processes in-the-wild images and targets at opening up a promising direction for practical applications of symmetry. The new benchmark, named Sym-PASCAL, is composed of 1435 natural images with 1742 objects derived from the PASCAL-VOC-2011 [17] segmentation dataset. Such a benchmark is closer to practical

applications with challenges far beyond those in existing datasets, including: (1) diversity of objects: multi-class objects with different illuminations and viewpoints; (2) multi-object co-occurrence: multiple objects exist in a single image; (3) part-invisibility: objects are partially occluded; and (4) complex backgrounds: the scenes where object located could be contextually cluttered.

The symmetry detection problem is treated as an imageto-mask learning task, where we explore the deep sideoutput residual network (SRN) that uses color images as inputs and directly outputs response images about object reflection symmetry. SRN is rooted in the holistically-nested edge detection (HED) network [18] but upgrades it by cascading multiple residual units (RUs) on the side-outputs, which are computed on different stages of convolutional layers with fully convolutional network [19]. The residual unit (RU) is designed to fit the error between the object ground-truth symmetry and the output of RU, which uses concatenate operations and residual decomposition to fuse convolutional features. It is computationally easier as it pursues the minimization of residuals among scales rather than combining multi-scale features to fit the ground-truth symmetry. SRN provides an effective way to model the association and complementary among multi-layer features. The RUs we defined not only significantly improve the performance of SRN, but also solve the learning convergence problem left by the baseline HED method. By cascading multiple RUs in a deep-to-shallow manner, the receptive fields of stacked RUs can adaptively match the symmetry

SRN is composed of a trunk network for feature learning and a branch network for hierarchical side-outputs processing. When multiple branch networks are added to the trunk network, SRN is upgraded to a multi-task side-output residual network (MT-SRN), where the trunk network is

W. Ke, J. Jiao and Q. Ye are with the School of Electronic, Electrical and Communication Engeering, University of Chinese Academy of Sciences, Beijing, 101408, China.

E-mail: kewei11@mails.ucas.ac.cn, {jiaojb, qxye}@ucas.ac.cn.

J. Chen and G. Zhao are with Center for Machine Vision and Signal Analysis, University of Oulu, FI-90014, Finland.

E-mail: jiechen@ee.oulu.fi, guoying.zhao@oulu.fi

shared by different image-to-mask tasks, and each branch network specifies a task. The use of a shared trunk network not only reduces the number of network parameters, but also improves network learning by collectively leveraging training samples from multiple tasks. SRN was first proposed in our CVPR 2017 oral paper [20], and is upgraded to multi-task SRN (MT-SRN) in this full version. With extended experiments about symmetry detection and edge detection, the general applicability of SRN to image-to-mask learning tasks is further validated. The contributions of this paper include:

- An object reflection symmetry benchmark, which spans challenges of diversity, multi-objects, partinvisibility, and various complex backgrounds, promoting the symmetry detection research to in-thewild scenes.
- A side-output residual network (SRN) that can effectively fit the errors between ground-truth and the outputs of the stacked RUs, enforcing the modeling capability to multi-layer convolutional feature fusion, achieving state-of-the-art symmetry detection performance.
- A multi-task side-output residual network (MT-SRN) that can perform joint symmetry and edge detection, showing not only the generality of SRN to image-tomask learning tasks but also the feasibility to train a shared deep network on datasets for similar tasks.

The reminder of this paper is organized as follows. Related work is reviewed in Section 2. Section 3 introduces the Sym-PASCAL dataset for in-the-wild object reflection symmetry detection. Section 4 and Section 5 detail the implementation of SRN and MT-SRN. Section 6 presents experimental evaluation, and Section 7 concludes the paper.

## 2 RELATED WORK

An object is reflection symmetric if it can be divided into two or more identical pieces that are arranged in an organized manner [10]. This means that an object is symmetric if there is a transformation that moves individual pieces of the object but does not change the overall shape. According to the way the pieces are organized and the type of transformation, an object has reflectional, rotational, and scale symmetry<sup>1</sup>, which respectively corresponds to the representation of skeleton, orientation and scale. In this paper, we involve the reflectional symmetry.

For the applicability and beauty, symmetry has attracted much attention of the computer vision community. The focus of symmetry detection spans from binary images [8], [21] to color object images [10], [13], [14], [15], while the symmetry detection approaches range from hand-crafted [22], [23], [24] to learning based [3], [13], [14], [15], [20].

1. An object has reflectional symmetry (line or mirror symmetry) if there is a line going through it which divides it into two pieces which are mirror images of each other. An object has rotational symmetry if the object can be rotated about a fixed point without changing the overall shape. An object has scale symmetry if it does not change shape when it is expanded or contracted.

#### 2.1 Benchmarks

In the early research, symmetry extraction is qualitatively evaluated on quite limited binary shapes [8]. Such shapes are selected from the MPEG-7 Shape-1 dataset for subjective observation [21], or a few real-world images for objective evaluation [10]. SYMMAX [13] contains hundreds training/test images with reflection symmetry annotations, which can be regarded as an authentic benchmark. However, the reflection symmetry in SYMMAX mainly focuses on low-level image features, regardless of objects. WH-SYMMAX [14], SK506 [15], and SK-LARGE [16] are recently proposed benchmarks with annotation of object skeletons. Nevertheless, WH-SYMMAX is simply composed of sideview horses while SK506 and SK-LARGE consist objects with little background. Neither of them involve multiple objects or complex background, leaving a plenty of room for developing new object symmetry benchmarks.

In the proposed Sym-PASCAL benchmark, we emphasize the challenging aspects including object diversity, multi-objects, part-invisibility, and various complex backgrounds. We also provide Toolbox and instructions about how to create the dataset and define criteria about how to determine whether an image contains multiple objects and/or partial invisibility.

#### 2.2 Methods

Conventional methods: Early symmetry extraction methods, also referred to as skeleton detection<sup>2</sup> [9], [25], are mainly developed for binary images by leveraging morphological operations. When processing color images, they usually need a contour extraction or an image segmentation step as pre-processing [21], [26]. Considering that segmentation of in-the-wild images remains a research problem, the integration of image segmentation with symmetry detection not only increases the complexity but also accumulates the errors.

Researchers have tried to extract symmetry in color images based on multi-scale super-pixels [22], [23], [24]. One hypothesis is that object symmetry axes are the subsets of lines connecting center points of super-pixels [22]. Such line subsets could be explored from super-pixels using a sequence of deformable disc models to extract the symmetric path [23]. Their consistency and smoothness can be modeled with spatial filters, *e.g.*, a particle filter, which link local skeleton segments into continuous curves [24]. Due to a lack of object prior and an end-to-end learning module, these methods are limited to handling the images with simple backgrounds.

More effective approaches are rooted in powerful learning methods, where the object symmetry detection is treated as a per-pixel binary prediction problem, which becomes an image-to-mask task with dense prediction for all image pixels. On the SYMMAX benchmark, multiple instance learning (MIL) [13] is used to train a symmetry detector with multiscale and multi-orientation features. To capture diversity of symmetry patterns, the structured random forest (SRF) [3]

2. Although symmetry is equal to skeleton in most cases, it is different from skeleton when the objects have small length-width ratio or occlusion, Fig. 2c, and thus is a more accuracy word than skeleton in this paper.

and subspace MIL [14] is employed to train a symmetry detector with the same feature. Nevertheless, due to the limitation of the hand-designed features and conventional learning models, these methods are unable to detect the symmetry pixels with large scales, as much more context information needs to handle.

Deep learning methods: With the rise of deep learning, researchers have recently investigated the skeleton detection problem by fusing multi-layer convolutional features [15], [20]. This problem is later converted into the image-to-mask learning problem and unified with edge detection [18], [27], [28], [29], [30] and semantic segmentation [19], [31]. By using learned weights to combine the multi-layer convolutional features, object skeletons/edges/segments is extracted in an end-to-end manner.

DeepContour [27] and HED [18] are two pioneering works that use learned weights to fuse the multi-scale convolutional features and predict edges in an end-to-end manner. The trunk network of HED is a FCN [19], [32], which provides multi-scale convolutional features for multi-scale edge detection. When using the convolutional features in an oriented/encoder-decoder manner, HED is upgraded to detect oriented/higher-level object contours [28], [29]. Bertasius *et al.* [30] further show that they can predict object edges by exploiting object-level features from a multi-scale side-output network.

FCN is also be applied to semantic segmentation in an image-to-mask manner, *i.e.*, taking the input of arbitrary size images and producing the correspondingly-sized output [19]. The application of FCN to semantic segmentation not only validates its applicability to spatially dense prediction tasks [32], but also contributes to multi-task deep networks, *e.g.*, the multi-task network cascade [33] and joint object detection and semantic segmentation. In these works, multi-scale convolutional features are usually used in a cascading manner, while the problems about how to minimize the errors among multiple scales and adaptively fit complex outputs with limited convolutional layers need to be further explored.

Most recently, fusing scale-associated deep side-outputs (FSDS) [15] is shown to be capable of learning multiscale object skeleton representations on WH-SYMMAX and SK506. FSDS takes the architecture of HED [18] and supervises the side-outputs of HED with scale-associated ground-truth. Despite of its good performance on skeleton/symmetry detection, it needs the intensive annotations of the scales for each symmetry point, which means that it uses much more human efforts than other approaches when preparing the training data. Compared with FSDS, our proposed SRN can adaptively match the scales of symmetry, without requiring scale-associated annotation.

Multi-task learning: The concept of multi-task learning (MTL) is early proposed by Caruana [34]. Recently, multi-task deep learning that aims to solve multiple tasks using a single network has attracted increased attention [35], [36], [37], [38]. Sermanet *et al.* [35] use a CNN network for joint localization, detection, and classification. Eigen and Fergus [36] propose a multi-scale CNN for simultaneously predicting depth, surface normal, and semantic labels for an image. Eigen *et al.* [37] train a network for joint person detection, pose estimation, and gender recognition. These

methods have the advantage of performing multiple tasks with single deep networks, but are difficult to be trained by diverse datasets.

In this paper, SRN is extended to multi-task SRN (MT-SRN), which is trained on two diverse datasets. Compared with UberNet that fuses low-level, mid-level, and high-level vision tasks with diverse datasets, MT-SRN uses a different training strategy. It leverages a trunk network to extract low-level features, buffer convolutional layers to integrate the low-level features for task-specific purpose, and SRNs to calculate outputs on the buffer convolutional layers.

## 3 OBJECT SYMMETRY BENCHMARK

## 3.1 Annotation Toolbox

To facilitate symmetry annotation, we create a toolbox <sup>3</sup>, Fig. 1a. With the toolbox, annotators can simultaneously load images and masks, revise the masks, and save the ground-truth symmetry. Symmetry annotation involves pixel-level fine details, and is time-consuming. Our toolbox leverage the instance semantic segmentation and a skeleton generation algorithm to aid the annotation of symmetry [26]. With the toolbox, an annotator can complete the symmetry for an image within one minute.

The annotation instruction is defined and illustrated in Fig. 1b. First, it is required to load an image and its instance segmentation mask, Fig. 1b-(i). Second, it is required to use the "Disc" or "Poly" operations defined in the toolbox to obtain an extended mask, Fig. 1b-(ii). The skeletonazaition is applied on the extended mask to get initial reflection symmetry, Fig. 1b-(iii). Finally, it is required to cut the extended skeleton according to the original mask. The instances are annotated one by one and the ground-truth symmetry of whole image is completed, Fig. 1b-(iv).

## 3.2 Categorization

The released Sym-PASCAL is derived from the PASCAL-VOC-2011 segmentation dataset [17] which contains 1112 training images and 1111 test images from 20 object classes including: person, bird, cat, cow, dog, horse, sheep, aero plane, bicycle, boat, bus, car, motorbike, train, bottle, chair, dining table, potted plant, sofa, and tv/monitor.

We categorize the 20 classes of objects into symmetry-available and symmetry-unavailable, Fig. 2. The objects that contain a lot of discontinuous parts in the segmentation masks are labeled symmetry-unavailable, including potted plants, dining tables, motorbikes, bicycles, chairs, and sofas., Fig. 2a. The other 14 object classes are labeled symmetry-available. Some of objects are slender and thus easy to annotate, Fig. 2b, and others with small length-width ratio or occlusion are difficult to annotate, Fig. 2c. In total, 648/787 images are selected and annotated from the PASCAL-VOC-2011 training and test sets. Among these images, 31.3% are multi-object, *i.e.*, more than one instance in a single image, and 45.6% are part-invisibility, *i.e.*, an instance or a part of an instance is occluded by itself and/or other instances, or out scope of the image.

For the images where object symmetry is obvious, *i.e.*, objects are composed of slender parts that are easy to

3. https://github.com/KevinKecc/SRN.

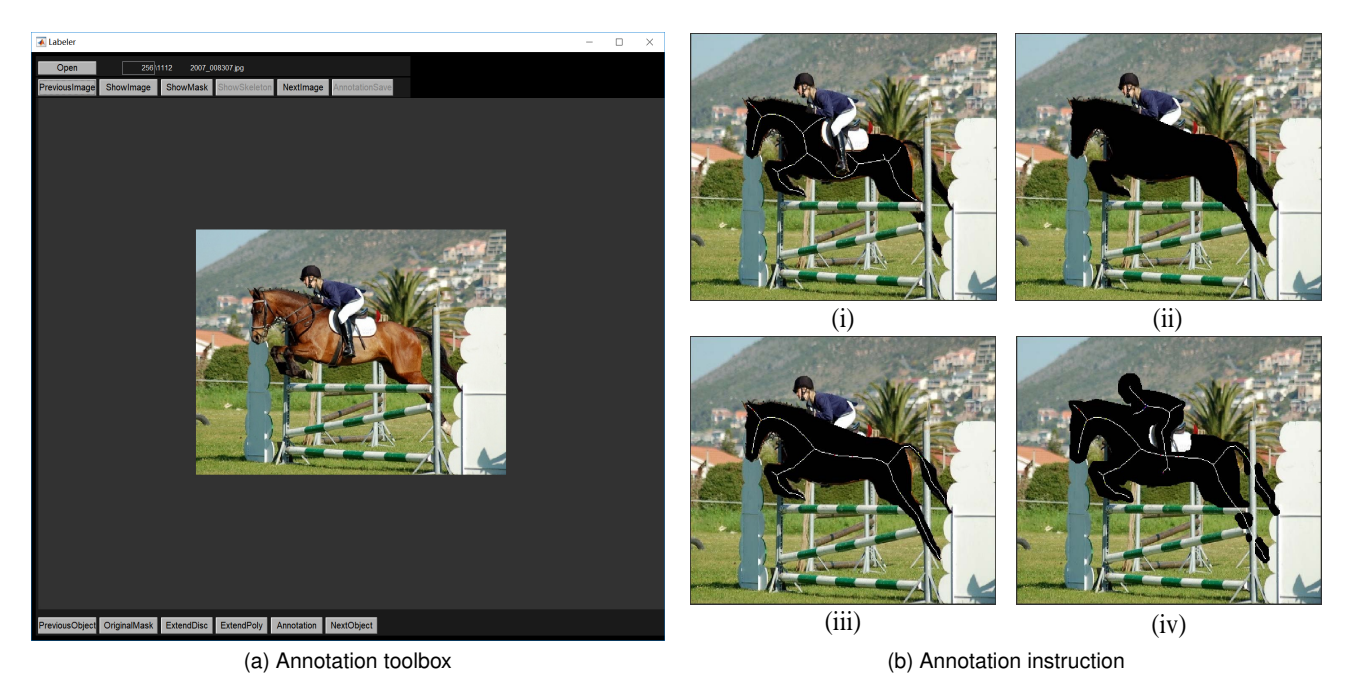


Fig. 1. Reflection symmetry annotation. (a) The annotation Toolbox. Its most salient aspect is the interactive function by which annotators can leverage instance semantic segmentation and skeleton generation algorithms to speed up symmetry annotation. (b) Annotation procedure: (i) Original mask and skeleton generation. (ii) Mannual mask extension. (iii) Reflection symmetry extraction for a single object. (iv) Reflection symmetry extraction for multiple objects.

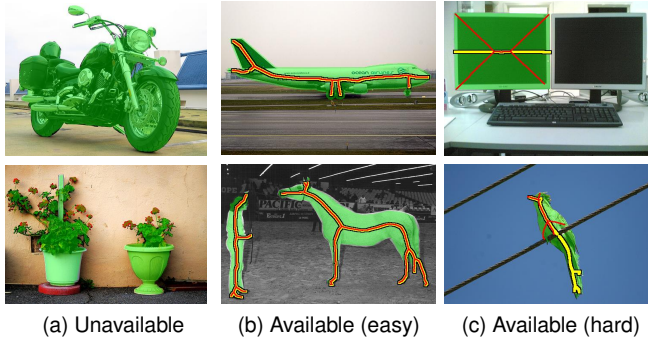


Fig. 2. Comparison of skeleton and object reflection symmetry. The green masks are annotated semantic segmentation ground-truth. The red lines are the skeletons of semantic segmentation masks. The yellow lines are the annotated symmetry ground-truth. (a) Symmetry unavailable images. (b) Images in which symmetry is equal to skeleton and is easy to be annotated. (c) Images in which symmetry is hard to be annotated. (Best viewed in color)

annotate, we directly extract symmetry on the object segmentation masks using a skeleton extraction algorithm [26], Fig. 2b. In these image, the object symmetry (marked with yellow curves) and their skeleton (marked with red curves) are consistent. For the images where object symmetry is not obvious, we manually extend the semantic segmentation masks and annotate symmetry on them, Fig. 2c. For a wide object on the top of Fig. 2c, we extend the mask along the direction of the long axis of the object and choose the long axis as ground-truth. For an occluded object at the bottom of Fig. 2c, we need to manually fill the missed parts of segmentation masks. For the images that contain partial objects, we empirically determine the occluded parts to extend the segmentation masks. With above processing, the skeleton extraction algorithm [26] is used to extract symmetry on the object segmentation masks. The object

TABLE 1
Comparison of Skeleton and Symmetry Detection Datasets.

	Data type	Image type	#object	#train -ing	#test -ing
SYMMAX	local symmetry	natural image	-	200	100
WH- SYMMAX	object skeleton	sample image	1	228	100
SK506	object skeleton	sample image	16	300	206
SK- LARGE	object skeleton	sample image	16	746	745
Sym- PASCAL	object symmetry	natural image	14	648	787

ground-truth symmetry is set as the skeleton points within the segmentation masks, marked with yellow curves in Fig. 2c.

## 3.3 Dataset comparison

In what follows, we compare the proposed benchmark with other four representative ones, SYMMAX [13], WH-SYMMAX [14], SK506 [15], and SK-LARGE [16].

SYMMAX is derived from BSDS300 [39], which contains 200/100 training and test images. It is annotated with local reflection symmetry on both the foreground and background. Considering that most computer vision tasks focus on the foreground [4], [40], it is more meaningful to compute the symmetry for objects (*i.e.*, foreground) instead of the symmetry for the whole image. WH-SYMMAX has 228 training images and 100 test images. It is developed for object skeletons, but it is made up of only cropped horse images, which are not comprehensive for general object

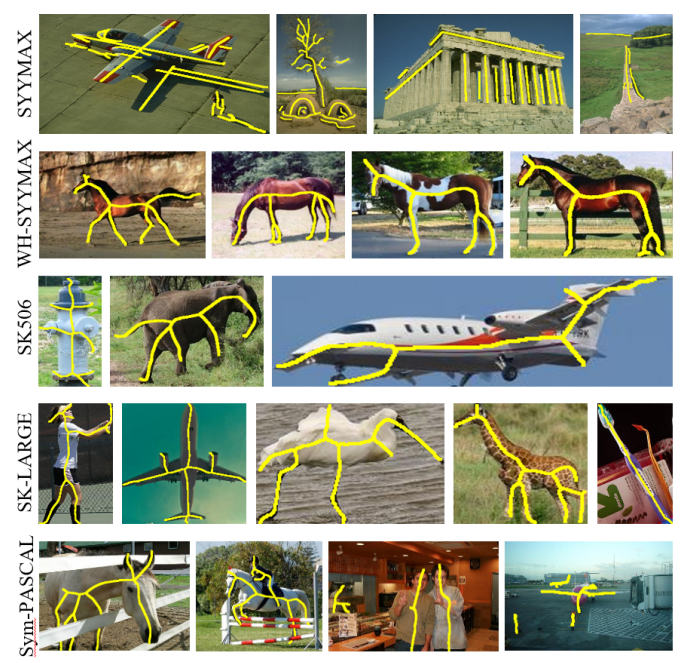
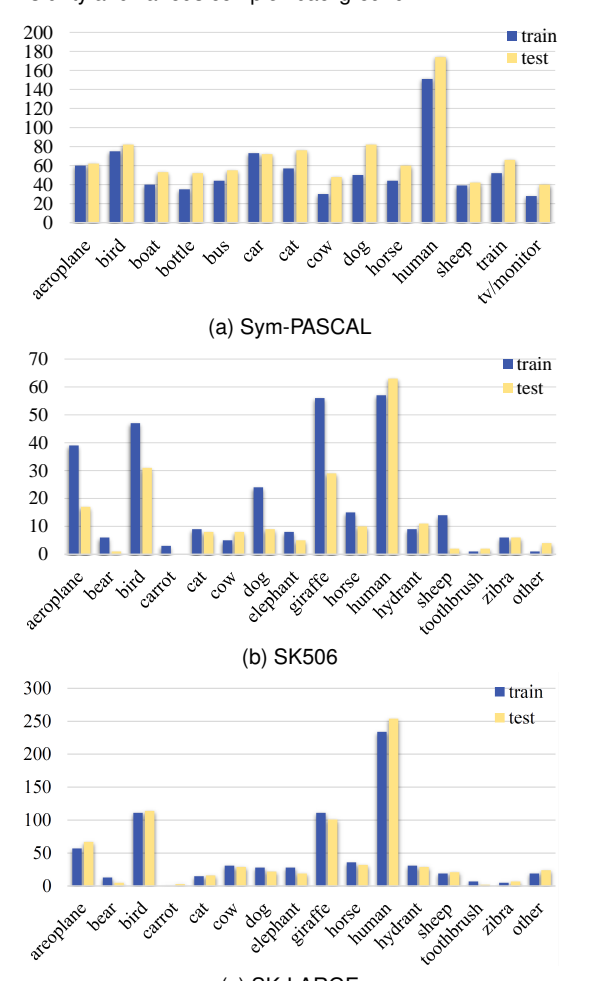


Fig. 3. Symmetry examples from the new released benchmark, Sym-PASCAL, and other four commonly used benchmarks. Compared with SYMMAX [13], WH-SYMMAX [14], SK506 [15], and SK-LARGE [16]. Sym-PASCAL spans challenges including object diversity, multi-objects, part-invisibility and various complex background.



(c) SK-LARGE Fig. 4. Object-class distributions of the Sym-PASCAL, SK506, and SK-LARGE datasets.

symmetry. SK506 involves skeletons from about 16 classes of objects with 300/206 training and test images. And SK-LARGE is extended from SK506 to 746/745 training and test images. Nevertheless, their backgrounds are too simple to represent in-the-wild images.

Some examples and the information of different symmetry datasets are shown in Fig. 3 and Table 1. As shown in Table 1. the proposed benchmark involves more training and test images. Particularly, these images involve complex backgrounds, multiple objects, and/or occlusions. It is developed for end-to-end object symmetry, providing a protocol to evaluate whether or not an algorithm can detect symmetry without additional object detectors. In Sym-PASCAL, the images for each class are more balanced than other datasets, Fig. 4a, except that the number of human objects is larger than others. In contrast, the object distributions of different classes have more unbalance in SK506 and SK-LARGE, Fig. 4b and Fig. 4c.

## 4 SIDE-OUTPUT RESIDUAL NETWORK

The proposed side-output residual network (SRN) is based on the simple but effective output residual unit (RU) and a deep-to-shallow learning strategy, Fig. 6. Given the ground-truth symmetry, the SRN is learned in an end-to-end manner

## 4.1 Output Residual Unit

Given training images, the end-to-end symmetry learning pursues deep network parameters that best fit the ground-truth symmetry. Such a learning objective is different from that of learning a classification network [41]. The RU defined for outputs, Fig. 5, is different from that in the residual network defined for features [41]. The former approximates a progressive estimation function for ground-truth while the latter eases the training of very deep networks. The idea of output residual is also successfully used in sparse coding [42].

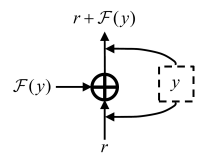
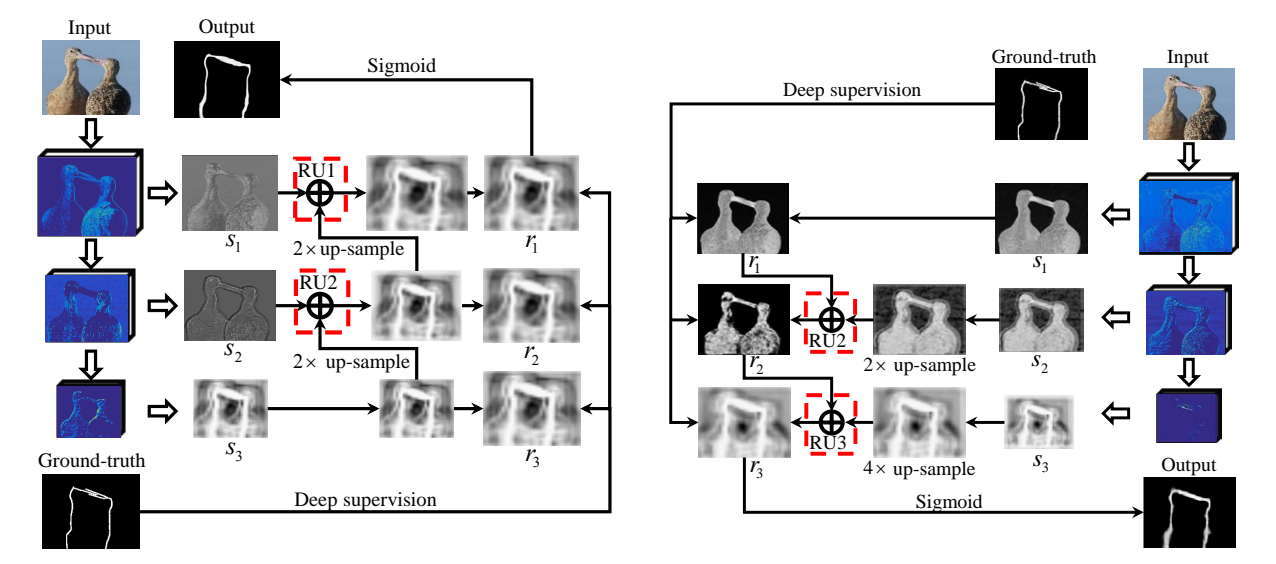


Fig. 5. The output Residual Unit (RU). By supervision both on the input and output of RU, the additional mapping  $\mathcal{F}(y)$  estimates the residual of ground-truth y.

For SRN, with the deep supervision both on the input and output of RUs, the residual of the ground-truth y is computed. Formally, denoting the input of a RU as r and the additional mapping as  $\mathcal{F}(y)$ , the deep supervision is written as

$$\begin{cases}
 r \approx y \\
 r + \mathcal{F}(y) \approx y
\end{cases} ,$$
(1)

where r and  $r + \mathcal{F}(y)$  are the input and output of the RU, respectively.  $\mathcal{F}(y)$  is regarded as the residual estimation of y. RUs provide shortcut connections between the ground-truth and outputs from different scales, which implies a functional module for the 'flow' of errors among different scales, and thus make it easier to fit complex outputs with higher adaptivity. To the extreme, if an input r is optimal, it



(a) Deep-to-shallow
(b) Shallow-to-deep
Fig. 6. The architectures of proposed side-output residual network (SRN) by cascading residual units (RUs) in (a) deep-to-shallow and (b) shallow-to-deep strategies. The RUs are marked with dashed boxes. With the deep supervision both on the input and output of RUi, i = 1, 2, 3, the residual between the ground-truth and the output of RUi (i.e.,  $r_i$ ) is computed hierarchically. Along the cascading orientation, the residual decreases so that the RUi (i.e.,  $r_i$ ) is closer to ground-truth than the input of RUi (i.e.,  $r_{i+1}$  in deep-to-shallow,  $r_{i-1}$  in shallow-to-deep).

would be easier to push  $\mathcal{F}(y)$  to zero than to fit it to ground-truth.

Given M RUs to be stacked, Eq. 1 is reformulated as

$$r_o = r_M + \sum_{i=M}^{1} \mathcal{F}_i(y), \tag{2}$$

where  $r_o$  is the final output of SRN and  $\{r_i\}_{i=1}^M \in [0, v_{gt}]$  are the inputs of RUs.  $v_{gt} \in \{0,1\}$  is the ground-truth. The M-th RU,  $r_M$ , is supervised by ground-truth and is seen as an initial approximated output. After the Sigmod operation, the residual is always positive, i.e.,  $\mathcal{F}_i(y)_{i=1}^M \geq 0$ , we have  $v_{gt} \geq r_o \geq r_1... \geq r_M$ , which means that the residual monotonically decreases in the order of the stacking RUs.

## 4.2 Network Architecture

By stacking the RUs defined, we implement a new kind of deep learning network, the side-output residual network (SRN), which incorporates the advantages of both the scale adaptability and residual learning. For SRN, the input of the first RU can be chosen as the deepest side-output or shallowest side-output, which derives two versions of SRN, Fig. 6. In what follows, the RU is numbered as the index of side-output, and the output of the i-th RU is denoted as  $r_i$ , for short.

**Deep-to-shallow:** In this SRN architecture, RUs are stacked from the deepest to the shallowest convolutional layer, Fig. 6a. The RUs are stacked so the input of one is set as the output of the former one. Sigmoid is used as classifier on the output of the last RU to generate output images.

The implementation of RU in the deep-to-shallow architecture is shown in Fig. 7a. Denote  $s_i$  the i-th side-output, and  $r_i+1$ ,  $r_i$  the input and output of i-th RU.  $s_i$  is used to learn the residual between  $r_{i+1}$  and the ground-truth, and update  $r_{i+1}$  to  $r_i$ . For the deepest RU, the input is set as the side-output, i.e.,  $r_3=s_3$ , Fig. 7a. Note that the size of output  $r_i$  in this architecture is the same as the side-output  $s_i$  rather than the size of input  $r_{i+1}$ . Therefore, a Gaussian

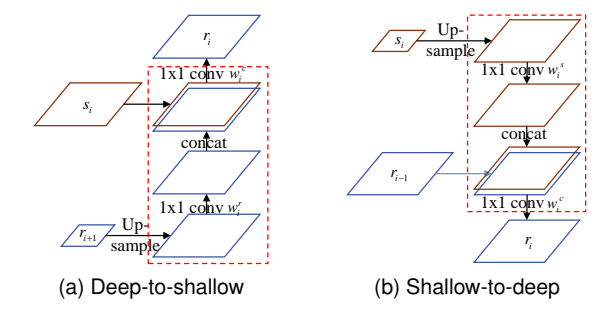


Fig. 7. The implementation of the *i*-th RU.

deconvolution layer [19] is introduced to up-sample  $r_{i+1}$ . In this architecture, only  $2\times$  up-sampling is used as the additional mapping, *i.e.*,  $\mathcal{F}(y)$ , is  $2\times$  large of the input of RU. As the up-sampling with fixed Gaussian kernel is a linear transformation, a weight layer  $w_i^r$  is used as soft-adding to improve the scale adaptability. Instead of hard-adding up-sampled  $r_{i+1}$  and  $s_i$  directly, a  $1\times 1$  convolutional layer  $w_i^c$  is utilized to generate  $r_i$ . The i-th RU is formulated as,

$$r_i = w_i^c \otimes (s_i + w_i^r \cdot r_{i+1}). \tag{3}$$

The convolution operation in Eq. 3 can be written as,

$$r_i = w_{i1}^c \cdot s_i + w_{i2}^c \cdot w_i^r \cdot r_{i+1}, \tag{4}$$

where  $w_i{}^c, w_i{}^r$  are the convolutional weights of the concatenation layer and the up-sampled  $r_{i+1}$ .  $w_i{}^r$  is a scaler to weight the  $r_{i+1}$  and  $w_i{}^c$  has two elements, one for  $s_i$  and the other for  $r_{i+1}$ . With Eqs. (1) and (4), the output residual  $\mathcal{F}_i(y)$  is computed, as

$$\mathcal{F}_i(y) = w_{i_1}^c \cdot s_i + (w_{i_2}^c \cdot w_i^r - 1)r_{i+1}. \tag{5}$$

When  $w_{i2}^c \cdot w_i^r$  approximates 1.0, the residual is related to only the side-output. To the extreme, along the stacking orientation of RUs, the residual  $\mathcal{F}(y)$  approximates 0.0.

**Shallow-to-deep:** The architecture is shown in Fig. 6b and the RU is shown in Fig. 7b. The side-outputs are upsampled by the Gaussian deconvolution layer so that their size is consistent with the input image. In the shallow-to-deep architecture, the input of RU has the same size with the input image, so  $2\times$  up-sampling is used for side-output of stage2 and  $4\times$  up-sampling is used for side-output of stage3. Similar to Eq. (5), the residual is computed, as

$$\mathcal{F}_i(y) = w_{i_1}^c \cdot w_i^s \cdot s_i + (w_{i_2}^c - 1)r_{i+1}, \tag{6}$$

where  $w_i^s$  is convolutional weight of the up-sampled  $s_i$ . Fig. 6b shows that the shallowest  $r_1$  has lots of false positive pixels compare to ground-truth as  $s_1$  represents local structure of the input image. Along the cascading stages, the RU3 reduces the residual so that the output of RU3, *i.e.*,  $r_3$ , are closer to ground-truth compared to the input of RU3, *i.e.*,  $r_2$ .

As we know, the deep layers of CNNs contain features that ignore the image details but capture high-level representations. Therefore, a deep layer is expected to be closer to the optimal solution than the shallow one. In the deep-to-shallow architecture, the deepest side-output is used as a good initialization for the ground-truth, therefore, the deep-to-shallow architecture outperforms the shallow-to-deep one, as shown in Section 6.1.

## 4.3 Learning

Given the object reflection symmetry detection training dataset  $S = \{(X_n, Y_n)\}_{n=1}^N$  with N training pairs, where  $X_n = \{x_j^{(n)}, j=1,\cdots,T\}$  and  $Y_n = \{y_j^{(n)}, j=1,\cdots,T\}$  are the input images and the ground-truth binary images with T pixels, respectively.  $y_j^{(n)} = 1$  denotes a symmetry pixel and  $y_j^{(n)} = 0$  denotes non-symmetry pixel. We subsequently drop the subscript n for notational simplicity, by considering each image independently, and denote  $\mathbf{W}$  as the parameters of the trunk network. Given a convolutional network with M side-outputs, the M-th side-output is set as the basic output, and M-1 RUs are used in the learning procedure. The architecture of Fig. 6a is used as an example, where M=3 and  $r_3$  is the basic output. Fig. 6b has similar formulation. For the basic output, the loss is computed with weighted entropy loss [18], as

$$\mathcal{L}_{b}(\mathbf{W}, w_{b}) = -\beta \sum_{j \in Y_{+}} \log \Pr(y_{j} = 1 | X; \mathbf{W}, w_{b})$$
$$- (1 - \beta) \sum_{j \in Y_{-}} \log \Pr(y_{j} = 0 | X; \mathbf{W}, w_{b}),$$
(7)

where  $w_b$  is the classifier parameter for the basic output.  $Y_+$  and  $Y_-$  denote the symmetry and non-symmetry ground-truth label sets, respectively. The loss weight  $\beta = |Y_+|/|Y|$ , and  $|Y_+|$  and  $|Y_-|$  denote the symmetry and non-symmetry pixel numbers, respectively.  $\Pr(y_j=1|X;\mathbf{W},w_b)\in[0,1]$  is the Sigmoid prediction of the basic output that measures how confident it is that the point is on the axis of the symmetry. For the i-th RU,  $i=M-1,\cdots,1$ , the loss is computed, as

$$\mathcal{L}_{i}(\mathbf{W}, \theta_{i}, w_{i}) = -\beta \sum_{j \in Y_{+}} \log \Pr(y_{j} = 1 | X; \mathbf{W}, \theta_{i}, w_{i})$$
$$- (1 - \beta) \sum_{j \in Y_{-}} \log \Pr(y_{j} = 0 | X; \mathbf{W}, \theta_{i}, w_{i})$$
(8)

where  $\theta_i = (w_i^c, w_i^s)$  is the convolutional parameter of the concatenation layers and side-output layers after the *i*-th RU.  $w_i$  is the classifier parameter for the output of the *i*-th RU. Suppose the weight of RU output is  $\alpha$ , the loss function for all the stacked RUs is obtained by

$$\mathcal{L}(\mathbf{W}, \theta, w) = \alpha_M \mathcal{L}_b(\mathbf{W}, w_b) + \sum_{i=M-1}^{1} \alpha_i \mathcal{L}_i(\mathbf{W}, \theta_i, w_i).$$
(9)

Finally, we learn the parameters for the trunk network and branch network, as

$$(\mathbf{W}^*, \theta^*, w^*) = \arg\min \mathcal{L}(\mathbf{W}, \theta, w). \tag{10}$$

In the test phase, given an image X, a symmetry prediction map is output by the last RU,

$$\hat{Y} = \Pr(y_i = 1 | X; \mathbf{W}^*, \theta^*, w^*).$$
 (11)

## 4.4 Understanding SRN

The proposed SRN leverages output residual units (RUs) to fit the errors between the object symmetry ground-truth and the input of RUs. By cascading RUs in a deep-to-shallow manner, SRN approximates a progressive estimation function, which has been successfully used in mechanics and control systems [43] and validated to be more effective than direct linear error estimation. With such progressive estimation, SRN exploits the 'flow' of errors among multiple scales to ease the problems of fitting complex outputs with limited convolutional layers, suppressing the complex backgrounds, and effectively matching object symmetry of different scales.

From the perspective of learning, SRN implements a special kind of learner ensemble, where each learner corresponds to a convolutional layer and can be regarded as a weak learner. Multiple weak learners are assembled to construct a strong learner. The deep-to-shallow SRN first chooses the best weak learner, which uses features from the deep convolutional layer to fit the ground-truth. In the next layer, the error of each sample is calculated and samples of larger error contributes more to the second weak learner. Such a procedure could be regarded as a special kind of re-sampling, by assigning larger weights to samples with larger errors. With weak learner ensemble and re-sampling, the learning procedure of SRN is a boosting-like algorithm [44].

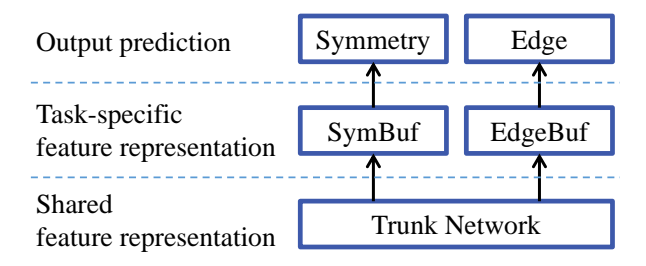


Fig. 8. General framework of the proposed multi-task side-output residual network (MT-SRN).

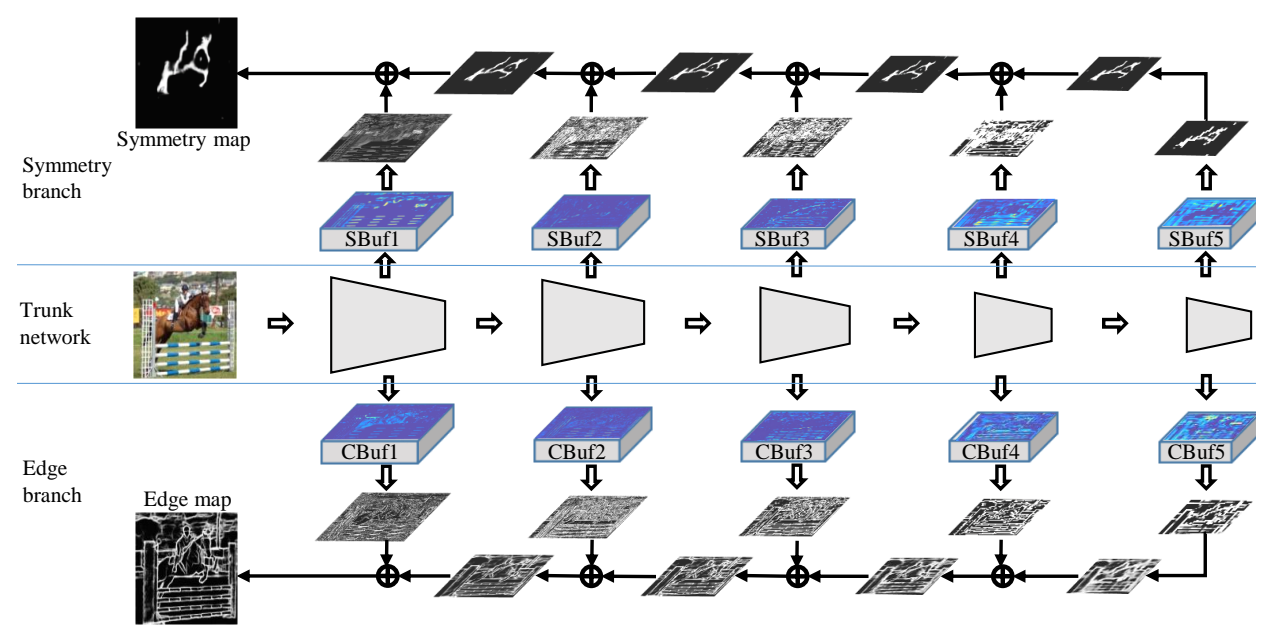


Fig. 9. Architecture of multi-task side-output residual network (MT-SRN). Buffer convolutional layers (CBuf and SBuf) are added to the trunk network to construct a symmetry branch network and an edge branch network. The MT-SRN is optimized with an alternating training strategy.

#### 5 MULTI-TASK SRN

SRN consists of a trunk network for feature learning and a branch network, i.e., stacked RUs, for hierarchically side-outputs processing. When multiple branch networks are added to the trunk, the SRN is upgraded to a multi-task SRN (MT-SRN), Fig. 8. In MT-SRN, the trunk network is used for shared feature representation, the buffer layers are for task-specific feature representation, and stacked RUs for output prediction. By combining multiple tasks we can use more data to train a shared trunk network to activate object regions and depress complex backgrounds. In this paper, MT-SRN is used to perform joint symmetry and edge detection by using a color image as input and taking Sigmoid processing on the output of the last stacked RU.

MT-SRN has two loss functions, defined as

$$\mathcal{L}_S = \mathcal{L}(\mathbf{W}_T, \theta_S, w_S), \tag{12}$$

$$\mathcal{L}_E = \mathcal{L}(\mathbf{W}_T, \theta_E, w_E), \tag{13}$$

where  $\mathbf{W}_T$  are the parameters of the trunk network;  $\theta_S$ ,  $\theta_E$  are the parameters of symmetry branch and edge branch, and  $w_S$ ,  $w_E$  are classifiers of the side outputs, respectively. To optimize the two loss functions defined, we propose an alternating training strategy,

$$(\mathbf{W}_T^*, \theta_S^*, w_S^*) = \arg\min \mathcal{L}(\mathbf{W}_T, \theta_S, w_S), \tag{14}$$

$$(\mathbf{W}_T^*, \theta_E^*, w_E^*) = \arg\min \mathcal{L}(\mathbf{W}_T, \theta_E, w_E).$$
 (15)

In the training phrase, we first fine-tune the trunk network with the edge branch, Eq. 14, and then fine-tune the trunk network with the symmetry branch, Eq. 15. Five training steps are used in total. The first step iterates 8,000 times, and the number of iterations is reduced by 2,000 for each step.

In the MT-SRN, the trunk network is shared for the two tasks that have different learning objectives. In the learning procedure, the network parameters could change drastically

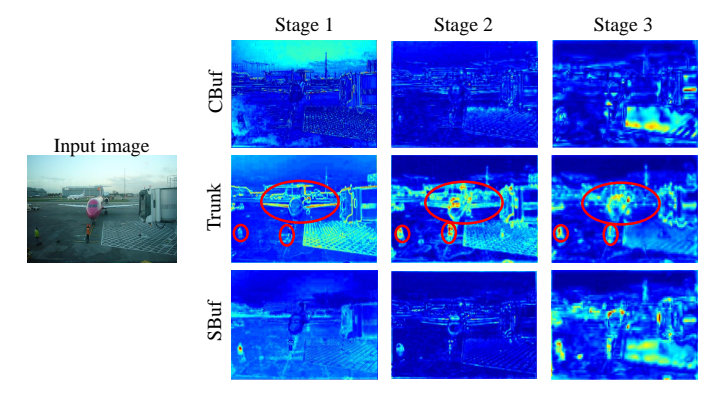


Fig. 10. The illustration of the activated pixels in MT-SRN. The trunk network tends to activate the object, and the Sbuf and Cbuf layers tends to activate edge pixel and symmetry regions, respectively. (Best viewed in color and zoomed in)

when switching between the loss functions defined in Eqs. (12) and (13), which aggregates the risk of leaning instability. To solve this problem, we propose inserting a buffer convolutional layer between each convolutional layer and sideoutput layer, Fig. 9. Buffer layers have been successfully used in a multi-scale region proposal network (RPN) [45] to alleviate the problem of sharp gradient values. In MT-SRN, the buffer layers are introduced to smooth the gradient values propagated from either branch network and guarantee that the parameters of the trunk network update smoothly. Besides, buffer layer is used to extrat the task-specfic feature. As shown in Fig. 10, the trunk network tends to activate the object regions and the Sbuf and Cbuf layers tends to activate edge pixel and symmetry regions, respectively.

The advantages of MT-SRN are twofold. i) In the training phase, the shared trunk networks of MT-SRN are fine-tuned by multiple datasets, e.g., the edge and symmetry datasets. This aggregates the limited training data from each dataset. ii) In the test phase, MT-SRN uses a shared

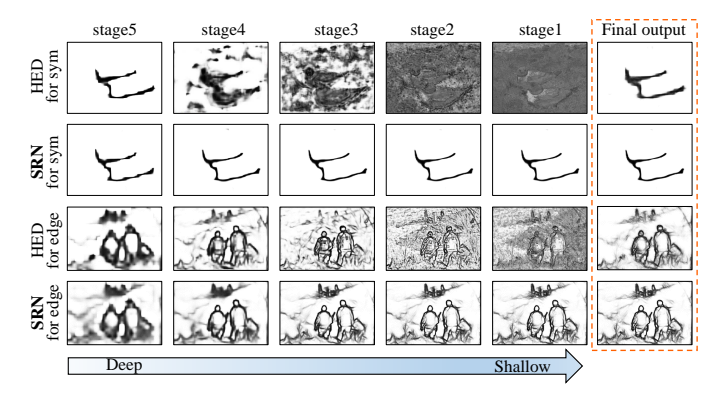


Fig. 11. Comparison of the side-outputs of HED [18] and the proposed SRN. From the first to the fifth collum we illustrate the side-outputs from deep to shallow stages. The last column is the final output. For SRN (the second and forth rows) it can be seen that the residuals between the outputs and the ground-truth decrease progressively. In contrast, HED (the first and third rows) has no such characteristic.

trunk network and forwards the trunk network once to perform two detection tasks. It saves both storage space and computational time compared to separated SRNs. The more tasks it performs, the more storage space and computational time it saves.

#### 6 EXPERIMENTS

In this section, the implementation of SRN for symmetry detection is first presented. The experimental results of symmetry detection are then analyzed and compared. Finally, the efficiency and effectiveness of using MT-SRN for joint symmetry and edge detection are validated.

SRN is built on the publicly available implementation of the deep network for holistically-nested edge detection, HED [18], by fine-tuning the pre-trained 16-layer VGG net [46]. A non-maximal suppression (NMS) algorithm [47] is applied on the final output map to obtain object symmetry or edge. The result difference between SRN and HED is illustrated in Fig. 11. The final output of HED is the average of weighted side-outputs, while that of SRN is achieved by cascading the side-outputs hierarchically from the deep to the shallow stages. As shown in the first and third rows of Fig. 11, the side-outputs from shallow stages of HED are about local structures and those from deep stages are about global contours. The weighted summing of multistage side-outputs in HED could introduce local noises to the final outputs. To alleviate the noise and preserve the global contours, the SRN stacks the multi-stage sideoutputs, with which the residuals between the RU-outputs and the ground-truth decrease progressively, as shown in the second and fourth rows of Fig. 11. This validates the monotonicity of residual in the order of the stacking RUs, as defined in Eq. 2.

## 6.1 SRN Implementation

*Parameters:* For both object reflection symmetry detection and edge detection, we set the mini-batch size to 1, the loss-weight  $\alpha$  to 1 for each RU side-output, the momentum to 0.9, the weight decay to 0.002, the maximum number of training iterations to 20,000, and the learning rate to 1e-8 for in-the-wile image datasets and 1e-6 for simple image datasets.

TABLE 2
Performance of SRN under Different Implementation on the Sym-PASCAL Benchmark.

Architecture	Augumentation   Conv1		F-measure	
	1×	with	0.381	
shallow-deep	1^	w/o 0.397		
	$0.8\times, 1\times, 1.2\times$	with	0.371	
	0.68,18,1.28	w/o	0.396	
	1×	with	0.443	
deep-shallow	1^	w/o <b>0.443</b>		
	$0.8 \times, 1 \times, 1.2 \times$	with	0.384	
		w/o	0.397	

Architecture: Table 2 shows that SRN with the deep-to-shallow architecture (F-measure 0.443) performs significantly better than the shallow-to-deep architecture (F-measure 0.397) on Sym-PASCAL dataset. It confirms that the deep-to-shallow architecture is easier to reduce the residual than the shallow-to-deep one as its initialization is better, as analyzed in Section 4.2.

Data Augmentation: Data augmentation can aggregate the training datasets. In this work, image rotation, flipping, upsampling, and down-sampling (multi-scale) are used for data argumentation, following [15]. For each scale, we rotate the training images every 90 degrees and flip them along different axis. The performance with/without multi-scale data argumentation is compared. Table 2 shows that the F-measure decreases when using multi-scale augmentation, even though it produces more training data. The reason is that the ground-truth symmetry is made up of curves with one-pixel thickness. The upsampling operation produces curves that have thickness lager than one pixel, and the down-sampling operation produces discontinuous symmetry curves.

Conv1: SRN is trained without conv1 stage of VGG because the size of receptive field is so small (only  $5\times 5$ ) that it introduces local noise of symmetry (too small to capture any symmetry response). The negative impact of a small receptive field with FSDS [15] is also observed. By pairwise comparison in Table 2, the F-measure without conv1 is slightly better than that with conv1.

#### 6.2 Symmetry Detection

*Datasets:* The proposed SRN is evaluated on both Sym-PASCAL and the other four datasets, *i.e.*, SYMMAX, WH-SYMMAX, SK506, and SK-LARGE. The different characteristics of these datasets have been compared in Section 3.

Evaluation Metrics: The precision-recall metric with F-measure is used to evaluate the performance of symmetry detection, as introduced in [13]. To obtain the precision-recall curves, the detected symmetry response is truncated by different thresholds into a binary map, and then matched with the ground-truth symmetry masks. By changing the threshold value, the precision-recall curve is obtained and the best F-measure is computed.

#### 6.2.1 Performance on Sym-PASCAL

Using the deep-to-shallow SRN with data augmentation but without conv1, we compared the performance of SRN with the state-of-the-art, Fig. 12 and Table 3. All the compared results are generated by running the open source codes with default parameter settings. We also compare the result of

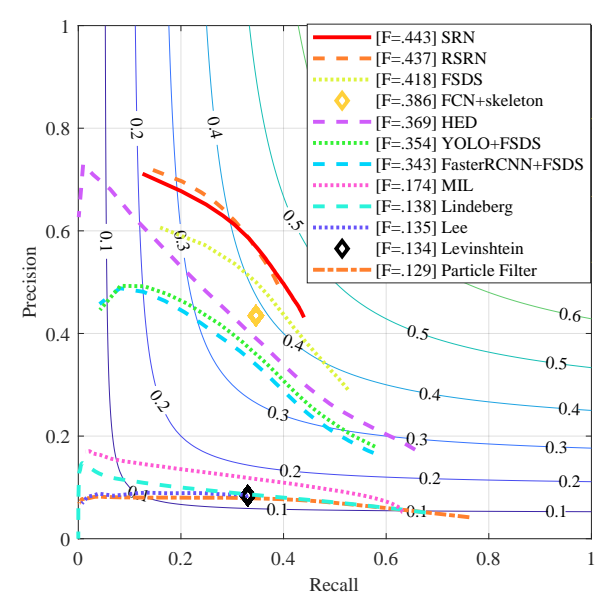


Fig. 12. Performance comparison on the Sym-PASCAL dataset.

TABLE 3
Performance comparison of the state-of-the-art approaches on the Sym-PASCAL dataset. †GPU time with NVIDIA Tesla K80

Methods		F-measure	Runtime/s
Conventional methods	Particle Filter [24]	0.129	25.3
	Levinshtein [22]	0.134	183.87
	Lee [23]	0.135	685.94
	Lindeberg [49]	0.138	5.79
	MIL [13]	0.174	80.35
Two-stage deep learning methods	Faster-RCNN [50] + FSDS [15]	0.343	0.33 †
	YOLO [51] + FSDS [15]	0.354	0.12 †
	FCN [19] + skeleton [26]	0.386	0.76 †
End-to-end deep learning	HED (baseline) [18]	0.369	0.10 †
	FSDS [15]	0.418	0.12 †
methods	SRN (ours)	0.443	0.12 †
memous	RSRN (ours)	0.437	0.13 †

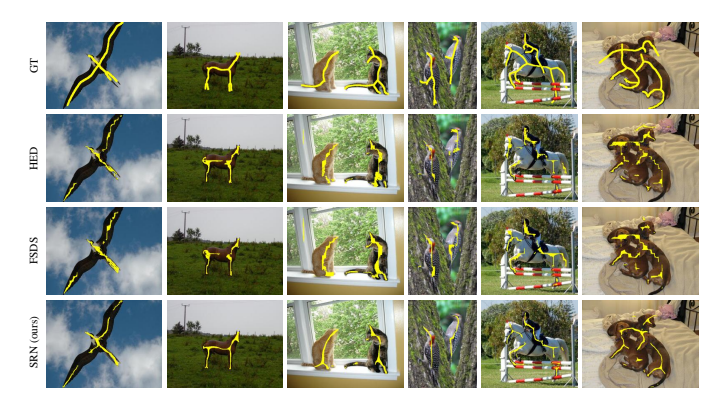


Fig. 13. Object reflection symmetry detection results on the Sym-PASCAL dataset: the first and second columns for one-object images with/without complex background, the third and forth columns for multi-object images with/without complex background, and the last two columns for images with occluded objects.

Rich-SRN (RSRN) [48], which we use all the 13 convolutionl layers of VGG.

In Table 3 One can find that the traditional methods perform poorly and are time consuming. The best F-measure of conventional methods is 0.174 by MIL [13], indicating the

challenge of the proposed benchmark. Lindeberg [49] runs fastest with 5.79s per image. Levinshtein [22], MIL [13], Lee [23], and Particle Filter [24] need much more running time for the complex features used.

The end-to-end deep learning methods perform significantly better than the conventional ones, both on the computational efficiency and detection performance, Table 3. Specifically, HED gets F-measure 0.369 and uses only ten milliseconds to process an image. FSDS degenerates to HED when the scale information is not used. Its F-measure reaches 0.418 when slicing and concatenating of each sideoutput are used. The proposed SRN and RSRN achieve the highest F-measure 0.443 and 0.437, which respectively outperform the baseline HED approach by 7.4% and 6.8% and the state-of-the-art FSDS approach by 2.5% and 1.9%.

The object reflection symmetry detection results of the state-of-the-art deep leaning approaches are illustrated in Fig. 13. From the first and second columns, it is observed that the object symmetry obtained by the proposed SRN approach is more consistent with the ground-truth with/without complex background for the images with one object. The third and fourth columns show examples that contain multiple objects, in which the proposed SRN approach achieves more accurate results than other approaches. The last two columns show the results of images with occluded objects and SRN also achieves the best results.

Comparison with two-stage approaches: To show the effectiveness of the end-to-end pipeline in complex backgrounds, we compare the proposed SRN with two-stage approaches composed of semantic segmentation/object detection and skeleton extraction. We choose a state-of-theart segmentation network FCN-8s [19] to localize objects, and the skeleton method [26] to extract symmetry, which obtains an F-measure of 0.386, as shown in Fig. 12. We also compare the FSDS [15] on the detection results from the state-of-the-art object detection methods, Faster-RCNN [50] and YOLO [51]. In these two approaches, the FSDS trained on SK506 is performed on object regions produced by Faster-RCNN or YOLO. As shown in Fig. 12, the Fmeasures are 0.343 and 0.354, respectively. Experimental results in Table 3 indicate that the proposed end-to-end learning approach is a more effective and efficient to detect object symmetry than the two-stage approaches. Comparing with the end-to-end SRN, two-stage approaches introduce error accumulation from the semantic segmentation and the object detection steps. Besides, semantic segmentation cannot obtain homogeneous masks when occlusion exists.

## 6.2.2 Results on Other Datasets

The performances on other three symmetry datasets are shown in Fig. 14 and Table 4. Similar to Sym-PASCAL, the deep learning based methods achieve significantly better performance on all the datasets than the traditional methods, especially for the simple image datasets, WH-SYMMAX, SK506, and SK-LARGE. Compared with the baseline HED, the proposed SRN improves F-measure from 0.427 to 0.446, 0.732 to 0.780, 0.542 to 0.632, 0.586 to 0.678 on SYMMAX, WH-SYMMAX, SK506, and SK-LARGE, respectively. RSRN further achieves 1.2% and 0.7% performance gain on WH-SYMMAX and SK-LARGE.

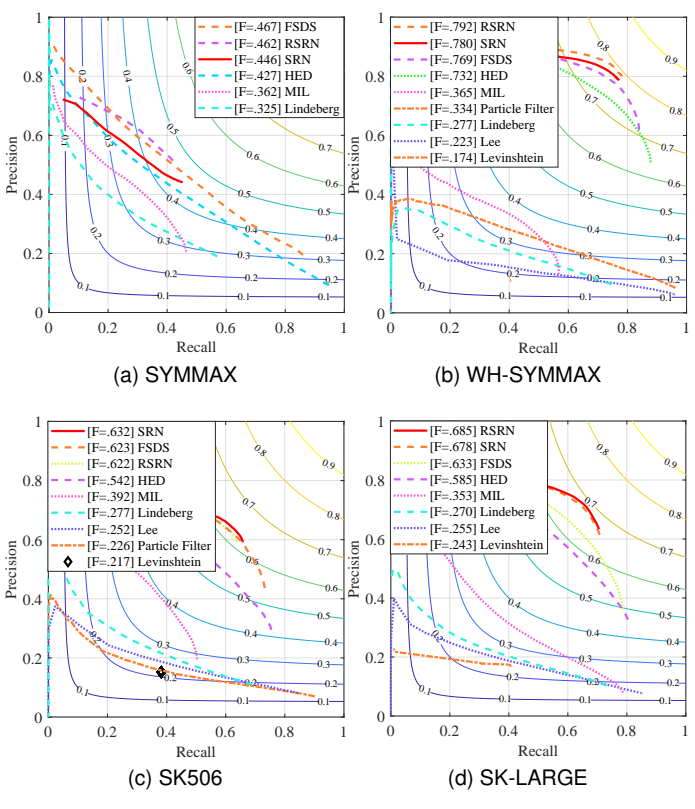


Fig. 14. The precision-recall curves for object reflection symmetry detection on the SYMMAX, WH-SYMMAX, SK506, and SK-LARGE datasets.

On WH-SYMMAX and SK506, we achieve the best performance. On SYMMAX, we achieve comparable performance with FSDS. On SK-LARGE, SRN is about 4% lower than Seg-Skel. We note that SegSkel uses semantic segmentation cues and is computationally complex.

TABLE 4
Performance Comparison of the State-of-the-art Approaches on the SYMMAX, WH-SYMMAX, and SK506 dataset.

datasets	SYMMAX	WH- SYMMAX	SK506	SK- LARGE
Levinshtein [22]	_	0.174	0.217	0.243
Lee [23]	_	0.223	0.252	0.255
Lindeberg [49]	0.360	0.277	0.227	0.270
Particle Filter [24]	_	0.334	0.226	_
MIL [13]	0.362	0.365	0.392	0.293
HED [18]	0.427	0.732	0.542	0.586
FSDS [15]	0.467	0.769	0.623	0.633
Seg-Skel [52]	_	_	_	0.730
SRN(ours)	0.446	0.780	0.632	0.678
RSRN(ours)	0.462	0.792	0.622	0.685

# 6.3 Edge Detection

The BSDS500 [39] dataset is used to evaluate the performance of edge detection, which is composed of 200 training, 100 validation, and 200 test images. Each image is manually annotated by five persons. For training images, we preserve their positive labels annotated by at least three human annotators, following [39]. Edge detection is evaluated with three standard measures [39]: fixed contour threshold (ODS) which is the same as F-measure, per-image best threshold (OIS), and average precision (AP).

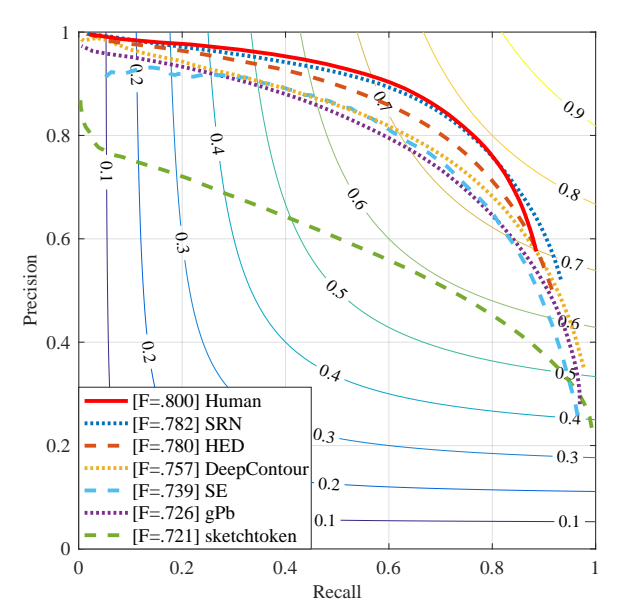


Fig. 15. Edge detection results on BSDS500.

TABLE 5 Edge Detection Results on BSDS500.

Methods	ODS	OIS	AP	FPS
Human	0.800	0.800	-	_
Canny [53]	0.590	0.620	0.578	15
Sketch Tokens [54]	0.721	0.739	0.768	1
SE [47]	0.739	0.759	0.792	2.5
DeepContour [27]	0.757	0.776	0.790	0.03
HED [18]	0.780	0.797	0.814	2.5
SRN (ours)	0.782	0.800	0.779	2.3

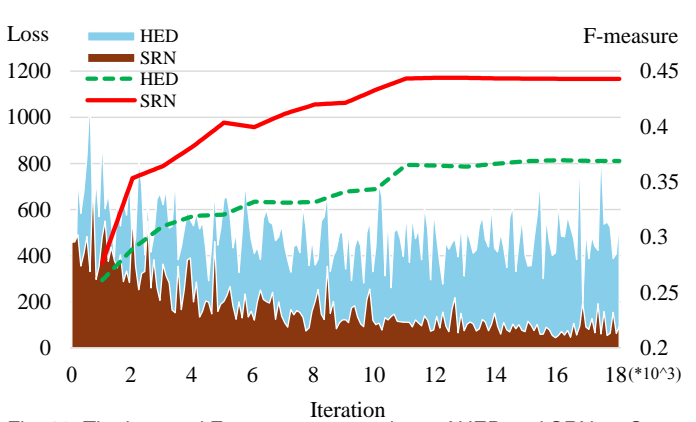


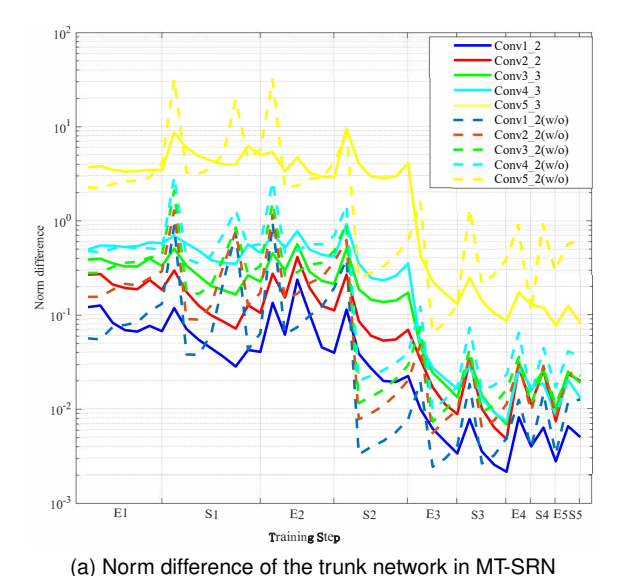
Fig. 16. The loss and F-measure comparison of HED and SRN on Sym-PASCAL.

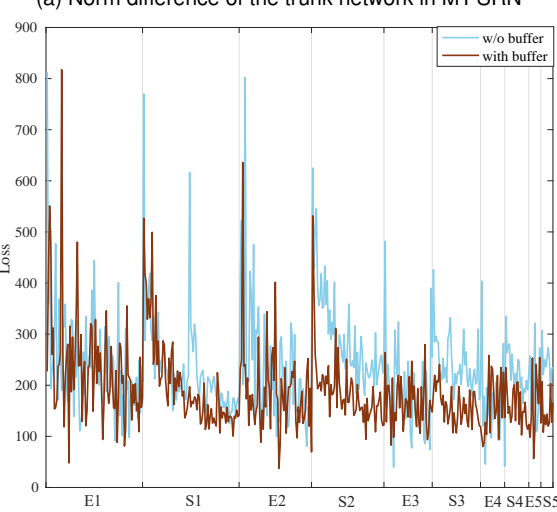
## 6.3.1 Performance

After the Sigmoid classification, the outputs from the last stacked RU produce edge masks, as shown in Fig. 15 and Table 5. In Table 5, the CNN-based methods significantly outperform the conventional methods. Specifically, Deep-Contour [27] has very good performance, but is computational expensive. The HED [18] achieves better performance with ODS=0.780, which is computed fast at 2.5 fps. With negligible computational cost overhead, the proposed SRN achieves ODS=0.782 at 2.3 fps, which outperforms the baseline HED method.

#### 6.4 Learning Convergence

The learning convergence of the baseline HED and the proposed SRN on Sym-PASCAL is shown in Fig. 16. It can





(b) Loss curve of MT-SRN Fig. 17. Comparison of norm difference (a) and loss curve (b) of MT-SRN with and without buffer layers.

Training Ster

be seen that the HED has a learning convergence problem, despite the fact that it gets good perfromace on edge and symmetry detection tasks. Benefiting from the output residual fitting, the loss curve of the proposed SRN tends to converge, Fig. 16. The HED needs 12,000 learning iterations to achieve the best performance. Benefits from the residual units (RUs), SRN needs only 3,000 iterations to achieve the same performance.

#### 6.5 Multi-task SRN

In MT-SRN, a 16-layer VGG is used as the trunk network, and the parameters of the buffer layers are the same as those of the connected convolutional layers in the trunk network. In total five training steps are run with 8,000, 6,000, 4,000, 2,000, and 1,000 learning iterations. In each training step, the edge and symmetry branches are trained alternatively, with a learning rate 1e-6 for the first two steps and 1e-8 for the last three steps.

As discussed in Section 5, the stability of the trunk network parameters in MT-SRN are important as they are related to learning convergence. Such stability is measured with the norm difference of the convolutional parameters

TABLE 6
Results of MT-SRN on Edge and Symmetry Detection Tasks.

	Datasets	ODS	F-measure
	Datasets	(edge)	(symmetry)
	BSDS500	0.782	_
	SYMMAX	_	0.446
SRN	WH-SYMMAX	_	0.780
	SK506	_	0.632
	SK-LARGE	_	0.678
	Sym-PASCAL	_	0.443
	(BSDS500, SYMMAX)	0.768	0.441
MT-	(BSDS500, WH-SYMMAX)	0.763	0.772
SRN	(BSDS500, SK506)	0.771	0.620
(w/o)	(BSDS500, SK-LARGE)	0.781	0.652
, ,	(BSDS500, Sym-PASCAL)	0.773	0.436
MT- SRN	(BSDS500, SYMMAX)	0.785	0.464
	(BSDS500, WH-SYMMAX)	0.779	0.807
	(BSDS500, SK506)	0.786	0.639
	(BSDS500, SK-LARGE)	0.786	0.681
	(BSDS500, Sym-PASCAL)	0.784	0.453

during the learning iterations. Fig. 17a shows that the stability decreases when training branch switches from one to another. For example, in the first learning stage when the learning switching from the edge branch to the symmetry branch at the 8,000-th iteration, the norm difference is large. It is also observed that after the five setps (E1 $\rightarrow$ S1, S1 $\rightarrow$ E2, ..., E5 $\rightarrow$ S5,) of learning, the difference decreases to a very small value. The decreasing norm difference signifies the increasing of the network stability, which not only validate the effectiveness of buffer layers but also the plausibility of MT-SRN. The norm difference of MT-SRN without buffer layer is also shown in Fig. 17a, which oscillates larger than the MT-SRN with buffer layer. It results in that the loss of MT-SRN without buffer layer is not convergence as good as the MT-SRN with buffer layer, Fig. 17b.

We use the datasets above for symmetry and edge detection to evaluate the performance of MT-SRN, Table 6. Surprisingly, the performances for both tasks increase. When BSDS and SYMMAX are used for joint edge and symmetry detection, the ODS of edge detection is improved from 0.782 to 0.785 and F-measure of symmetry detection improves from 0.446 to 0.464, which updates the state-of-the-arts, Table 6. The other four groups of datasets, *i.e.*, (BSDS500, WH-SYMMAX), (BSDS500, SK506), (BSDS500, SK-LARGE), and (BSDS500, Sym-PASCA), have the similar improvement. There are two reasons for the performance improvement. One is that more training iterations (42,000) are used for the trunk network so that MT-SRN is trained better than individual SRN (20,000 iterations). This advantage is observed by comparing with specific task with a singular dataset in Fig. 16, the F-measure of SRN doesn't increase with more iterations. The other is that two different datasets mean more training images so that the diversity of the training set increases. The fact that more training data can improve the performance is illustrated in object detection when multiple datasets for a single task are combined [50]. We further validate that the proposed MT-SRN is feasible to train a shared deep network on datasets from different image-tomask tasks, which is very useful for tasks where there is no significant training data available.

In Table 6, it can be seen that the MT-SRN with buffer layers reports higher performance than MT-SRN witout

buffer layers for both object reflection symmetry detection and edge detection, as the buffer layer is used as a feature transformation function, and each pixel has task-specific feature representation.

The general applicability presented by MT-SRN is using a shared trunk network and separated buffer layers to perform multi-task learning. This helps build deep learning models that can save both storage space and computational cost. Specifically, two separated SRN models need 115, 060 KB space, whereas the MT-SRN model needs 78,966 KB. MT-SRN saves 36,094 KB.

# 7 CONCLUSION

Symmetry detection has great applicability in computer vision yet remains unsolved, as indicated by the low performance (often lower than 50%) of the state-of-the-art methods. In this work, we release a new benchmark for object reflection symmetry, and propose the side-output residual network (SRN), establishing a strong baseline for object symmetry reflection detection in-the-wild. The new benchmark, with challenges related to real world images, is validated to be a good touchstone of various state-ofthe-art approaches. The proposed SRN, with well-defined and stacked residual units (RUs), is validated to be more effective to perform symmetry detection in complex backgrounds. With the adaptability to object scales, the robustness to complex backgrounds, and the end-to-end learning architecture, we extend the SRN to process a similar imageto-mask computer vision task, i.e., edge detection. With multiple network branches designed and alternating training strategy proposed, SRN is further upgraded to multitask SRN (MT-SRN) for joint symmetry and edge detection, showing great potential to process the image-to-mask tasks lack of training data.

#### **ACKNOWLEDGMENTS**

The authors would like to express their sincere appreciation to Prof. David Doermann and Dr. Pengxu Wei for their comments and suggestions. This work is partially supported by NSFC under Grant 61671427 and 61771447, and Beijing Municipal Science and Technology Commission under Grant Z181100008918014. Tekes, Academy of Finland and Infotech Oulu are also gratefully acknowledged. Qixiang Ye is the corresponding author of this paper.

## REFERENCES

- [1] T. B. Sebastian, P. N. Klein, and B. B. Kimia, "Recognition of shapes by editing their shock graphs," IEEE Trans. Pattern Anal. Mach. Intell., vol. 26, no. 5, pp. 550-571, 2004.
- N. H. Trinh and B. B. Kimia, "Skeleton Search: Category-specific object recognition and segmentation using a skeletal shape model," Int. J. Comput. Vis., vol. 94, no. 2, pp. 215–240, 2011.
- C. L. Teo, C. Fermüller, and Y. Aloimonos, "Detection and segmentation of 2D curved reflection symmetric structures," in Proc. IEEE
- Int. Conf. Comput. Vis. (ICCV), Dec. 2015, pp. 1644–1652. H. Fu, X. Cao, Z. Tu, and D. Lin, "Symmetry constraint for foreground extraction," IEEE Trans. Cybern., vol. 44, no. 5, pp. 644– 654, 2014.
- T. S. H. Lee, S. Fidler, and S. J. Dickinson, "Learning to combine mid-level cues for object proposal generation," in Proc. IEEE Int. Conf. Comput. Vis. (ICCV), Dec. 2015, pp. 1680-1688.
- X. Bai, X. Wang, L. J. Latecki, W. Liu, and Z. Tu, "Active skeleton for non-rigid object detection," in Proc. IEEE Int. Conf. Comput. Vis. (ICCV), Sep. 2009, pp. 575-582.

- [7] Z. Zhang, W. Shen, C. Yao, and X. Bai, "Symmetry-based text line detection in natural scenes," in Proc. IEEE Int. Conf. Comput. Vis. Pattern Recognit. (CVPR), Jun. 2015, pp. 2558-2567.
- L. Lam, S. Lee, and C. Y. Suen, "Thinning methodologies A comprehensive survey," *IEEE Trans. Pattern Anal. Mach. Intell.*, vol. 14, no. 9, pp. 869-885, 1992.
- P. K. Saha, G. Borgefors, and G. S. di Baja, "A survey on skeletonization algorithms and their applications," Pattern Recognit. Lett., vol. 76, pp. 3-12, 2016.
- [10] J. Liu, G. Slota, G. Zheng, Z. Wu, M. Park, S. Lee, I. Rauschert, and Y. Liu, "Symmetry detection from realworld images competition 2013: Summary and results," in Proc. IEEE Int. Conf. Comput. Vis. Pattern Recognit. Workshop, 2013, pp. 200-205.
- [11] Y. Liu, H. Hel-Or, C. S. Kaplan, and L. J. V. Gool, "Computational symmetry in computer vision and computer graphics," Found. and *Trends in Comput. Graph. and Vis.*, vol. 5, no. 1-2, pp. 1–195, 2010.
- [12] S. Lee and Y. Liu, "Curved glide-reflection symmetry detection," IEEE Trans. Pattern Anal. Mach. Intell., vol. 34, no. 2, pp. 266-278,
- [13] S. Tsogkas and I. Kokkinos, "Learning-based symmetry detection in natural images," in Proc. Europ. Conf. Comput. Vis. (ECCV), Oct. 2012, pp. 41-54.
- [14] W. Shen, X. Bai, Z. Hu, and Z. Zhang, "Multiple instance subspace learning via partial random projection tree for local reflection symmetry in natural images," *Pattern Recognit.*, vol. 52, pp. 306– 316, 2016.
- [15] W. Shen, K. Zhao, Y. Jiang, Y. Wang, Z. Zhang, and X. Bai, "Object skeleton extraction in natural images by fusing scale-associated deep side outputs," in Proc. IEEE Int. Conf. Comput. Vis. Pattern Recognit. (CVPR), Jun. 2016, pp. 222-230.
- [16] W. Shen, K. Zhao, Y. Jiang, Y. Wang, X. Bai, and A. L. Yuille, "Deepskeleton: Learning multi-task scale-associated deep side outputs for object skeleton extraction in natural images," IEEE Trans. Image Process., vol. 26, no. 11, pp. 5298–5311, 2017.
- C. K. I. Williams, (2011) The PASCAL Everingham, L. Van Gool, C. Winn, and A. Zisserman. Visual Object Classes Challenge 2011 (VOC2011) Results. [Online]. Available: http://www.pascal-network.org/challenges/ VOC/voc2011/workshop/index.html
- [18] S. Xie and Z. Tu, "Holistically-nested edge detection," in Proc. IEEE
- Int. Conf. Comput. Vis. (ICCV), Dec. 2015, pp. 1395–1403.
  [19] J. Long, E. Shelhamer, and T. Darrell, "Fully convolutional networks for semantic segmentation," in Proc. IEEE Int. Conf. Comput. Vis. Pattern Recognit. (CVPR), Jun.2015, pp. 3431-3440.
- [20] W. Ke, J. Chen, J. Jianbin, Z. Guoying, and Q. Ye. (2017) SRN: Side-output residual network for object symmetry detection in the wild. [Online]. Available: https://arxiv.org/abs/arXiv:1703.02243
- [21] X. Bai, L. J. Latecki, and W. Liu, "Skeleton pruning by contour partitioning with discrete curve evolution," IEEE Trans. Pattern Anal. Mach. Intell., vol. 29, no. 3, pp. 449-462, 2007.
- [22] A. Levinshtein, C. Sminchisescu, and S. J. Dickinson, "Multiscale symmetric part detection and grouping," Int. J. Comput. Vis, vol. 104, no. 2, pp. 117-134, 2013.
- [23] T. S. H. Lee, S. Fidler, and S. J. Dickinson, "Detecting curved symmetric parts using a deformable disc model," in Proc. IEEE Int. Conf. Comput. Vis. (ICCV), Dec. 2013, pp. 1753-1760.
- [24] N. Widynski, A. Moevus, and M. Mignotte, "Local symmetry detection in natural images using a particle filtering approach, IEEE Trans. Image Process., vol. 23, no. 12, pp. 5309-5322, 2014.
- [25] Z. Yu and C. L. Bajaj, "A segmentation-free approach for skeletonization of gray-scale images via anisotropic vector diffusion," in Proc. IEEE Int. Conf. Comput. Vis. Pattern Recognit. (CVPR), Jun. 2004, pp. 415-420.
- W. Shen, X. Bai, R. Hu, H. Wang, and L. J. Latecki, "Skeleton growing and pruning with bending potential ratio," Pattern Recognit., vol. 44, no. 2, pp. 196-209, 2011.
- [27] W. Shen, X. Wang, Y. Wang, X. Bai, and Z. Zhang, "Deepcontour: A deep convolutional feature learned by positive-sharing loss for contour detection," in Proc. IEEE Int. Conf. Comput. Vis. Pattern Recognit. (CVPR), Jun. 2015, pp. 3982-3991.
- S. Hallman and C. C. Fowlkes, "Oriented edge forests for boundary detection," in Proc. IEEE Int. Conf. Comput. Vis. Pattern Recognit. (CVPR), Jun. 2015, pp. 1732–1740.
- [29] J. Yang, B. L. Price, S. Cohen, H. Lee, and M. Yang, "Object contour detection with a fully convolutional encoder-decoder network," in Proc. IEEE Int. Conf. Comput. Vis. Pattern Recognit. (CVPR), Jun. 2016, pp. 193-202.

- [30] G. Bertasius, J. Shi, and L. Torresani, "High-for-low and low-for-high: Efficient boundary detection from deep object features and its applications to high-level vision," in *Proc. IEEE Int. Conf. Comput. Vis. (ICCV)*, Dec. 2015, pp. 504–512.
- [31] G. Ghiasi and C. C. Fowlkes, "Laplacian pyramid reconstruction and refinement for semantic segmentation," in *Proc. Europ. Conf. Comput. Vis. (ECCV)*, Oct. 2016, pp. 519–534.
- [32] E. Shelhamer, J. Long, and T. Darrell, "Fully convolutional networks for semantic segmentation," *IEEE Trans. Pattern Anal. Mach. Intell.*, vol. 39, no. 4, pp. 640–651, 2017.
- [33] J. Dai, K. He, and J. Sun, "Instance-aware semantic segmentation via multi-task network cascades," in *Proc. IEEE Int. Conf. Comput. Vis. Pattern Recognit. (CVPR)*, Jun. 2016, pp. 3150–3158.
- [34] R. Caruana, "Multitask learning," *Mach. Learning*, vol. 28, no. 1, pp. 41–75, 1997.
- [35] P. Sermanet, D. Eigen, X. Zhang, M. Mathieu, R. Fergus, and Y. Le-Cun, "Overfeat: Integrated recognition, localization and detection using convolutional networks," in *Proc. IEEE Int. Conf. Learn. Representat. (ICLR)*, 2014, pp. 5454–5463.
- [36] D. Eigen and R. Fergus, "Predicting depth, surface normals and semantic labels with a common multi-scale convolutional architecture," in *Proc. IEEE Int. Conf. Comput. Vis. (ICCV)*, 2015, pp. 2650–2658.
- [37] R. Ranjan, V. M. Patel, and R. Chellappa, "Hyperface: A deep multi-task learning framework for face detection, landmark localization, pose estimation, and gender recognition," *IEEE Trans. Pattern Anal. Mach. Intell.*, 2017.
- [38] I. Kokkinos, "Ubernet: Training a universal convolutional neural network for low-, mid-, and high-level vision using diverse datasets and limited memory," in *Proc. IEEE Int. Conf. Comput. Vis. Pattern Recognit.* (CVPR), 2017, pp. 5454–5463.
- [39] P. Arbelaez, M. Maire, C. C. Fowlkes, and J. Malik, "Contour detection and hierarchical image segmentation," *IEEE Trans. Pattern Anal. Mach. Intell.*, vol. 33, no. 5, pp. 898–916, 2011.
- [40] A. Borji, M. Cheng, H. Jiang, and J. Li, "Salient object detection: A benchmark," *IEEE Trans. Image Process*, vol. 24, no. 12, pp. 5706– 5722, 2015.
- [41] K. He, X. Zhang, S. Ren, and J. Sun, "Deep residual learning for image recognition," in *Proc. IEEE Int. Conf. Comput. Vis. Pattern Recognit. (CVPR)*, Jun. 2016, pp. 770–778.
- [42] T. Zhang and F. Porikli, "Sparse coding on cascaded residuals," in *Proc. Asia Conf. Comput. Vis. (ACCV)*, Nov. 2016, pp. 19–34.
- [43] D. De Santis, "High-order linear and non-linear residual distribution schemes for turbulent compressible flows," *Comput. Methods in Appl. Mech. and Eng.*, vol. 285, pp. 1–31, 2015.
- [44] Y. Freund and R. E. Schapire, "Experiments with a new boosting algorithm," in *Proc. 13st Int. Conf. Mach. Learn. (ICML)*, Jul. 1996, pp. 148–156.
- [45] Z. Cai, Q. Fan, R. Feris, and N. Vasconcelos, "A unified multiscale deep convolutional neural network for fast object detection," in *Proc. Europ. Conf. Comput. Vis. (ECCV)*, Oct. 2016, pp. 354–370.
- [46] K. Simonyan and A. Zisserman, "Very deep convolutional networks for large-scale image recognition," in Proc. IEEE Int. Conf. Learn. Representat. (ICLR), 2015.
- [47] P. Dollár and C. L. Zitnick, "Fast edge detection using structured forests," *IEEE Trans. Pattern Anal. Mach. Intell.*, vol. 37, no. 8, pp. 1558–1570, 2015.
- [48] C. Liu, W. Ke, J. Jiao, and Q. Ye, "RSRN: rich side-output residual network for medial axis detection," in *IEEE International Conference* on Computer Vision Workshops, 2017, pp. 1739–1743.
- [49] T. Lindeberg, "Edge detection and ridge detection with automatic scale selection," Int. J. Comput. Vis., vol. 30, no. 2, pp. 117–156, 1998.
- [50] S. Ren, K. He, R. B. Girshick, and J. Sun, "Faster R-CNN: towards real-time object detection with region proposal networks," in Adv. in Neural Inf. Process. Syst. (NIPS), 2015, pp. 91–99.
- [51] J. Redmon, S. K. Divvala, R. B. Girshick, and A. Farhadi, "You only look once: Unified, real-time object detection," in *Proc. IEEE Int. Conf. Comput. Vis. Pattern Recognit. (CVPR)*, Jun. 2016, pp. 779–788.
- [52] X. Liu, P. Lyu, X. Bai, and M. Cheng, "Fusing image and segmentation cues for skeleton extraction in the wild," in *IEEE International Conference on Computer Vision Workshops*, 2017, pp. 1744–1748.
- [53] J. Canny, "A computational approach to edge detection," *IEEE Trans. Pattern Anal. Mach. Intell.*, vol. 8, no. 6, pp. 679–698, 1986.
- [54] J. Lim, L. Zitnick, and P. Dollár, "Sketch tokens: A learned midlevel representation for contour and object detection," in *Proc.*

IEEE Int. Conf. Comput. Vis. Pattern Recognit. (CVPR), Jun. 2013, pp. 3158–3165.